Sheffield Hallam University

Synergistic Homovalent and Heterovalent Substitution Effects on Piezoelectric and Relaxor Behavior in Lead-Free BaTiO3 Ceramics

NALLAGATLA, Venkata Raveendra, MAIER, Christian, GLETTLER, Jürgen, FETEIRA, Antonio <http://orcid.org/0000-0001-8151-7009>, REICHMANN, Klaus and DELUCA, Marco

Available from Sheffield Hallam University Research Archive (SHURA) at:

http://shura.shu.ac.uk/33875/

This document is the author deposited version. You are advised to consult the publisher's version if you wish to cite from it.

Published version

NALLAGATLA, Venkata Raveendra, MAIER, Christian, GLETTLER, Jürgen, FETEIRA, Antonio, REICHMANN, Klaus and DELUCA, Marco (2024). Synergistic Homovalent and Heterovalent Substitution Effects on Piezoelectric and Relaxor Behavior in Lead-Free BaTiO3 Ceramics. Journal of the European Ceramic Society, 44 (14): 116689.

Copyright and re-use policy

See http://shura.shu.ac.uk/information.html

Sheffield Hallam University Research Archive
http://shura.shu.ac.uk

Journal of the European Ceramic Society 44 (2024) 116689

Contents lists available at ScienceDirect

Journal of the European Ceramic Society

journal homepage: www.elsevier.com/locate/jeurceramsoc

Synergistic homovalent and heterovalent substitution effects on piezoelectric and relaxor behavior in lead-free $BaTiO_3$ ceramics

Venkata Raveendra Nallagatla [a,*], Christian Maier [b], Jürgen Glettler [b], Antonio Feteira [c], Klaus Reichmann [d], Marco Deluca [a,*]

[a] Silicon Austria Labs GmbH, Sandgasse 34, Graz A-8010, Austria
[b] Materials Center Leoben Forschung GmbH, Roseggerstrasse 12, Leoben A-8700, Austria
[c] Materials and Engineering Research Institute, Sheffield Hallam University, Sheffield S1 1WB, United Kingdom
[d] Institute for Chemistry and Technology of Materials, Graz University of Technology, Stremayrgasse 9, Graz A-8010, Austria

ARTICLE INFO

Keywords:
Lead-free ferroelectrics
Barium titanate
Dielectric spectroscopy
Raman spectroscopy
Large-signal piezoelectric properties
Relaxors

ABSTRACT

This study investigates lead-free $BaTiO_3$ (BT) perovskite ceramics, unraveling the synergistic effects arising from simultaneous homovalent (Zr) and heterovalent (Nb) substitution. Focusing on piezoelectric, ferroelectric, and relaxor behaviors, this research employs a comprehensive suite of analyses, including temperature-dependent dielectric measurements, polarization-electric field hysteresis loops, and bipolar strain measurements. Significantly, our study unveils that the simultaneous substitution of Zr and Nb in the BT lattice induces room-temperature relaxor behavior at relatively low concentrations (5 % Zr and 3 % Nb), yielding higher permittivity and larger maximum polarization compared to single element (Zr or Nb) substituted BT relaxors. Bipolar strain measurements showcase substantial large-signal d_{33}* values (~250 pm/V) across a broad temperature range (–50 °C to 30 °C) for BT ceramics with simultaneous 5 % Zr and 2 % Nb substitution. This research advances understanding of homovalent and heterovalent substitution in BT ceramics and opens avenues for tailoring properties to suit specific applications.

1. Introduction

Barium titanate ($BaTiO_3$, BT), a classical lead-free ferroelectric (FE) material, exhibits the ABO_3 perovskite structure [1]. BT assumes an ideal cubic perovskite structure above approximately 130 °C (Curie Temperature, T_C), with the relative dielectric permittivity following the Curie-Weiss law [2]. Below T_C, BT undergoes two FE-FE phase transitions: first from tetragonal (P4mm) to orthorhombic (Amm2) at 6–12 °C, followed by a subsequent structural transition from orthorhombic to rhombohedral (R3m) at –77 to (–92) °C [1,3,4].

Implementing a chemical substitution strategy enhances BT dielectric performance tailored for specific applications, such as elevated material constants (permittivity, pyro- and piezoelectric coefficients), superior thermal stability across a wide temperature range, and the modulation of polarization-electric field (*P-E)* and dielectric constant-field (ε-*E*, i.e. tunability) hysteresis loops [3–6]. This enhancement can be achieved through homovalent (with charge 4+) or heterovalent (with charge 3+ or 5+) cation substitutions at the Ti-site of BT [7–10]. As the initial substituent content increases (e.g., Zr^{4+} or Nb^{5+}), the temperatures of the phase transitions between the FE phases rise, converging with the decreasing T_C at the so-called "tricritical point" [11]. With higher substituent contents, a diffuse phase transition (DPT) occurs from a rhombohedral FE to a cubic paraelectric phase [12,13]. Upon further substitution, relaxor behavior emerges, characterized by Vogel–Fulcher-like frequency dispersion of the temperature corresponding to the permittivity maximum, (T_m), and dissociating T_C from structural phase transitions [14]. While relaxors exhibit cubic symmetry on a macroscopic scale, the local-scale structure retains its polar nature to some extent [15]. Both DPT and relaxors present a slim hysteresis loop with higher permittivity close to room temperature, which makes them interesting for energy storage applications [12,16].

The manifestation of DPT or relaxor behavior, along with the corresponding polar order in BT perovskite, is intricately linked to the type of substitution applied [5]. Generally, the larger ionic radius of homovalent substituents induces random strain fields that hinder *B*-site displacements, disrupting the long-range FE order and thus slimming down the P-E loop [10,17]. Conversely, heterovalent substitutions introduce complexity by triggering various charge compensation mechanisms to

* Corresponding authors.
E-mail addresses: venkata.nallagatla@silicon-austria.com (V.R. Nallagatla), marco.deluca@silicon-austria.com (M. Deluca).

https://doi.org/10.1016/j.jeurceramsoc.2024.116689
Received 28 March 2024; Received in revised form 13 June 2024; Accepted 20 June 2024
Available online 21 June 2024
0955-2219/© 2024 The Authors. Published by Elsevier Ltd. This is an open access article under the CC BY license (http://creativecommons.org/licenses/by/4.0/).

maintain lattice electroneutrality [18,19]. In such cases, the disruption of B-site correlation (and the related effects on the P-E loop) occurs through a FE domain pinning mechanism. This pinning mechanism is due to random-field defects created by polar defects in the lattice, which induce robust lattice disorder and lead to relaxor behavior [20,21]. In our previous study [7], we delved into the origins of relaxor behavior in BT ceramics through homovalent ($BaZr_xTi_{1-x}O_3$—BZrT) and heterovalent ($BaNb_xTi_{1-x}O_3$—BNbT) solid solutions. The disruption of the long-range spatial correlation of Ti-cation displacements, a pivotal mechanism driving the emergence of relaxor behavior in BT-based perovskites, revealed distinct origins for homovalent and heterovalent substituents. Remarkably, heterovalent substitution (Nb^{5+}) proved more effective in inducing relaxor behavior with a minimal substitution concentration of ~7 %, compared to homovalent substitution (35 % of Zr^{4+}) in BT. In fact, the presence of B-site vacancies (V''''_{Ti}, in Kroger–Vink notation), and thus the presence of V''''_{Ti}-4 Nb^{5+} defect clusters in BNbT ceramics, proven in our previous study, is expected to create strong polar random fields (RFs), influencing the direction of Ti^{4+} and Nb^{5+} cation displacements in the neighboring unit cells. This effect induces robust lattice disorder, leading to relaxor behavior even with a minimal amount of heterovalent substituent concentration. In contrast, in BZrT, only strain effects arise from differences in ionic radii, giving rise to non-polar regions, with the extent of this effect significantly smaller than the observed strain and electrostatic potential difference in BNbT. Therefore, a substantially higher concentration of homovalent substituents is required compared to heterovalent substitution to induce relaxor behavior. In previous works, only B-site substitutions with one of those elements were investigated; to the best of the authors' knowledge, a systematic investigation of simultaneous Zr/Nb substitution in BT ceramics is still missing. The simultaneous Zr/Nb substitution in the BT lattice presents an intriguing avenue for tuning macroscopic dielectric, FE, and piezoelectric properties. It can be hypothesized that with a small amount of simultaneous Zr/Nb substitution, the strong RFs from V''''_{Ti}-4 Nb^{5+} defects (polar nature) may interact with external electric fields on a larger length scale than non-polar strain-based RFs resulting from Zr^{4+}, making the combination of both cations even more effective in disrupting Ti-O long-range correlation. Consequently, relaxor behavior could be induced at lower substituent contents than BNbT, allowing simultaneous avoidance of solubility issues and reduction of leakage current by shielding charged defects with (Zr-centered) non-polar regions.

This study delves into the intricate effects of concurrent Zr and Nb substitution in BT perovskite ceramics, with a specific emphasis on piezoelectric, FE, and relaxor behaviors. Employing a systematic methodology involving three distinct substitution series, we explored the influence of different Zr and Nb ratios on the structure, microstructure, and electrical properties.

2. Experimental

2.1. Sample preparation

$BaZr_xNb_yTi_{(1-x-5y/4)}O_3$ ceramics were prepared via the conventional solid-state mixed oxide method. To achieve the desired compositions, precise amounts of high-purity raw materials were weighed with an analytical balance, including electronic-grade $BaCO_3$ (Solvay Bario e Derivati, Italy; SSA = 3.3 m^2 g^{-1}), TiO_2 (Toho, Japan; SSA = 6.1 m^2 g^{-1}), Nb_2O_5 (99.9 % purity, H.C. Starck,; SSA = 6.3 m^2 g^{-1}, ceramic grade), and ZrO_2 (grade TZ0, Tosoh, Japan; SSA = 15.3 m^2 g^{-1}). The mixing process involved wet mixing these raw materials with zirconia grinding media in the presence of deionized water. Given the heterovalent (Nb^{5+}) doping, it was necessary to account for charge compensation; Ti deficiency was taken into account to promote the formation of Ti vacancies (V''''_{Ti}, in Kroger–Vink notation). Following the initial mixing and wet processing, the powders underwent calcination at 1250°C for 5 hours, and subsequently they were granulated by adding 5 %weight of polyethylene glycol, pressed, and sintered at temperatures from 1400°C to 1450°C for 5 hours in oxygen atmosphere, depending on the specific composition being targeted. To replenish oxygen vacancies, a subsequent reoxidation annealing process was carried out at 1000 °C for 48 hours in oxygen atmosphere.

2.2. Sample characterization

Powder XRD analyses were conducted using the D2 Phaser instrument (Bruker, Germany) equipped with a Co-K_α source, employing increments of 0.02° per step within the 20° to 80° 2θ range. Raman measurements were performed using a WITec alpha300R spectrometer (WITec GmbH, Ulm, Germany) with an 1800 gr/mm grating and an EC Epiplan-Neofluar DIC objective (Zeiss, Germany), utilizing a 532 nm laser excitation with an intensity of 10 mW. Scanning Electron Microscope (SEM) images, coupled with energy-dispersive X-ray spectroscopy (EDX), were acquired using the Crossbeam 340 instrument (Zeiss, Germany). Temperature-dependent dielectric properties were investigated employing an Agilent 4184 A precision LCR meter over a temperature range of −100 °C to 200 °C and at various frequencies spanning 10 Hz to 10 MHz. *P-E* and strain-electric field (*S-E*) loops were measured with a frequency of 10 Hz using an aixACCT TF 2000E tester with laser interferometer, covering temperatures ranging from –100 °C to 200 °C.

3. Results and discussion

Fig. 1 presents the XRD patterns of $BaZr_xNb_yTi_{(1-x-5y/4)}O_3$ (BZNT *x*-*y*, here *x* and *y* are corresponding substitutions amount - in %mole - of Zr and Nb, respectively) ceramic samples, highlighting three distinct series with varying Zr/Nb ratio substitutions, as follows: Series-1 maintains a constant Nb content (*y*) at 2.5 %, while systematically increasing the Zr content (*x*) to 10 %, 20 %, 30 %, and 40 %. In Series-2, the Zr content (*x*) remains fixed at 10 %, while the Nb content (*y*) undergoes incremental changes to 2.5 %, 5 %, 7 %, and 10 %. Series-3 holds the Zr content (*x*) at 5 %, progressively increasing the Nb content (*y*) to 1 %, 2 %, 3 %, and 5 %. All series of sintered ceramic samples exhibited the typical perovskite structure, which is confirmed by the XRD patterns as shown in Fig. 1. Furthermore, the (200) peaks in 2theta, ranging from 43° to 47°, exhibited a gradual shift towards lower angles, signifying an expansion in lattice constant as Zr and Nb substitutions progressed in Series-1 and 2, respectively. The presence of (002) and (200) peaks in Fig. 1b and d confirms the coexistence of tetragonal and cubic symmetry in the ceramics at room temperature (RT). Within Series-1, only the (002) peak is evident for ceramics containing over 10 % Zr, indicating the absence of a tetragonal phase. In contrast, the merging of $(002)_T$ and $(200)_C$ peaks with increasing Nb content in Series-2 suggests a gradual shift from tetragonal to cubic symmetry. At RT, the BZNT ceramics may exhibit various structural phases, including rhombohedral, orthorhombic, tetragonal, and cubic, depending on the Zr/Nb content. Unlike other investigative techniques such as Raman spectroscopy [22], which is more suitable at discerning subtle changes in local crystalline order, the coherence length of XRD proves insufficient to resolve minute distortions even adopting a refinement process. Nevertheless, lattice parameters and unit cell volumes were derived through XRD Rietveld refinement, as depicted in Figure S1 of the supporting information (SI). As anticipated, in both Series-1 and −2, the c lattice parameter (derived from the refinement of the tetragonal or cubic phase fraction) and unit cell volume exhibited a linear increase owing to the larger ionic radius of Zr^{4+} (0.72 Å)/Nb^{5+} (0.65 Å) in comparison to Ti^{4+} (0.605 Å) cations. Additionally, the merging of (002) and (200) peaks, along with the corresponding phase fraction values for tetragonal and cubic symmetry were identified, which is presented in Table S1 of the SI. The initial BZNT 10–2.5 ceramic displayed approximately 34.3 % tetragonal and 65.7 % cubic phases, while the XRD patterns of the subsequent samples in Series-1 could be accurately fitted with only cubic symmetry. In

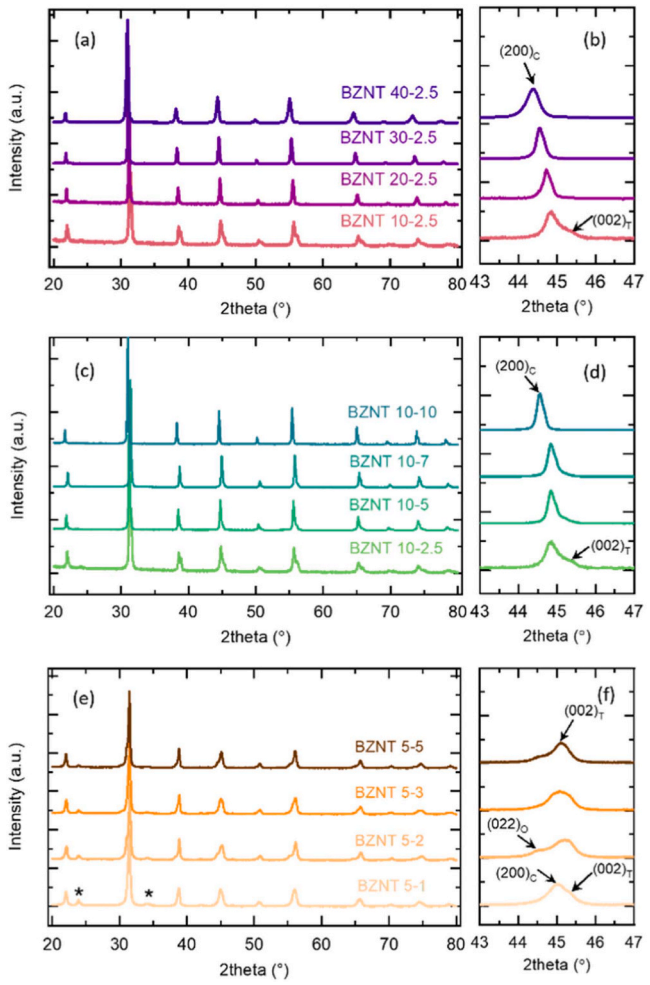

Fig. 1. XRD Patterns of BZNT at room temperature: (a) Series-1 with constant Nb content (y) at 2.5 %, showcasing the variation in Zr content (x = 10 %, 20 %, 30 %, and 40 %). (c) Series-2 with constant Zr content (x = 10 %) and increasing Nb content (y = 2.5 %, 5 %, 7 %, and 10 %). (f) Series-3 with constant Zr content (x = 5 %) and increasing Nb content (y = 1 %, 2 %, 3 %, and 5 %). (b), (d), and (f) provide detailed 2θ regions of the (002)/(200) reflections, ranging from 43° to 47° in (a), (c), and (e), respectively.

Series-2, a phase fraction of tetragonal and cubic symmetry persisted with increasing Nb content. However, the c/a ratio (tetragonality) of those ceramics is close to 1.0002, indicating a disordered pseudocubic phase.

In contrast, the XRD pattern of Series-3 samples revealed a subtle intensity of a secondary phase peak, denoted by an asterisk symbol in Fig. 1e, corresponding to residual $BaCO_3$, as identified by JCPDS no. 45–1471. The presence of $BaCO_3$ in those ceramics may be attributed to an incomplete calcination process or accuracy limitations in weighing (A/B ratio > 1). Fig. 1f illustrates the evolution of $(002)_T$, $(022)_O$, and $(200)_C$ peaks with increasing Nb content. These peaks exhibited a complex behavior, suggesting the presence of a mixture of two or three phases in Series-3 ceramics. The lattice constant of Series-3 ceramics obtained from XRD Rietveld refinement are presented in Figure S1c. The calculated c lattice parameter, derived from the tetragonal or cubic phase fraction, exhibited a linear increase with increasing Nb content, consistent with the trends observed in Series-2. Although the coherence length of XRD is insufficient to resolve small distortions (such as the local pseudocubic phase, or tetragonal and orthorhombic phases) for slight changes in Nb content, a qualitative XRD phase analysis was performed using Rietveld refinement, and phase fraction values are detailed in Table S1. The initial BZNT with 5 % Zr and 1 % Nb ceramic showed ~95 % tetragonal and ~5 % cubic phases, while BZNT 5–2 or BZNT 5–3 ceramics exhibited a blend of tetragonal (~76 % or 63 %, respectively) and orthorhombic (14 % or 27 %, respectively) phase fractions. For the highly Nb-substituted BZNT 5–5 ceramics XRD pattern, Rietveld refinement was unable to be performed with two phases; it necessitated a combination of tetragonal, orthorhombic, and cubic phases. It is noteworthy that, based on our Raman analysis (discussed in Fig. 7 below), no rhombohedral symmetry was observed. Therefore, rhombohedral phase fraction contribution was excluded in the Rietveld XRD refinement.

Fig. 2 presents SEM images showcasing the microstructures of selected samples within Series-1, Series-2, and Series-3. Top of Form

A comprehensive microstructural analysis of all the samples can be found in Figure S2 of the SI. The microstructures of these samples exhibit a remarkable level of uniformity, homogeneity, and high density. The grain size distribution and average grain size are presented in the insets accompanying the corresponding SEM images. It is evident that, within Series-1, there is a modest increase in grain size, transitioning from 1.50 μm to 1.70 μm from 10 % Zr to 40 % Zr content, respectively. Similarly, Series-2 samples also display a relatively modest increase in grain size, progressing from 1.50 μm to 1.60 μm from 2.5 % Nb to 10 % Nb content, respectively. In stark contrast, Series-3 samples experience a significant reduction in grain size, plummeting from 3.25 μm to 1.10 μm with an increase in Nb substitution from 2.5 % to 5.0 %. This observation underscores the inhibitory effect of Nb substitution on grain growth in BZNT samples, which apparently is active only at low Zr contents. This effect is attributed to the diffusion of Nb into BT grain cores, resulting in the formation of Ti-rich grain boundaries and the subsequent suppression of grain growth [23]. The presence of (111) twins is noticeable in the SEM micrograph of BZNT 10–2.5 and BZNT 5–2 ceramics, as shown in Figs. 2a and 2d, respectively. These (111) twins are observed only in some grains, while they are rarely observed in BZNT 5–1 matrix grains. Similar twins are frequently found in BT ceramics and are attributed to the presence of a Ti-rich liquid phase above the eutectic temperature [24–26]. It was observed that BT ceramics substituted with 3 % of Nb inhibited anomalous grain growth, potentially hindering the formation of twin-like microstructures in higher Nb-doped ceramics [27].

Fig. 3 presents the relative permittivity as a function of temperature at various frequencies ranging from 10 Hz to 10 MHz for all the samples under investigation. Within Series-1, the maximum permittivity peak (ε_m) gradually shifts to lower temperatures with increasing Zr substitution, as illustrated in Fig. 3a. Intriguingly, the frequency-dependent dispersion of the ε_m peak as a function of temperature (T_m), spanning over many orders of magnitude in frequency, becomes apparent already in the initial BZNT 10–2.5 sample, indicative of its relaxor behavior. It's worth noting that ε_m peaks shifted down to well below –100 °C for higher Zr substitutions (beyond 20 %), which lies below the minimum temperature limit of our experimental setup, rendering ε_m peaks beyond this point unrecordable. Similarly, in Series-2, the ε_m peak also exhibited a pronounced shift well below –100 °C for samples with higher Nb substitutions (above 2.5 %), as depicted in Fig. 3b. Notably, the threshold substitution concentration for relaxor behavior varies significantly between single-substituted (BZrT or BNbT) systems and their double-substituted counterpart (BZNT). In single-substituted systems, the threshold concentration is 7 % for heterovalent (BNbT) and 35 % Zr in homovalent (BZrT) systems [7]. The relaxor behavior in the double substituted BZNT system manifests itself even with Zr and Nb substitution concentrations of 10 % and 2.5 %, respectively, demonstrating the effectiveness of co-substitution for achieving relaxor behavior.

In an effort to tailor the ε_m peak to align with near RT, and thus to achieve high dielectric and piezoelectric performance close to RT, Series-3 samples were prepared with a constant Zr substitution of 5 %, while incrementally increasing the Nb concentration from 1 % to 5 %. The ε_r as a function of temperature, probed at frequencies ranging from 10 Hz to 10 MHz, is depicted in Fig. 3c. BZNT 5–1 and BZNT 5–2

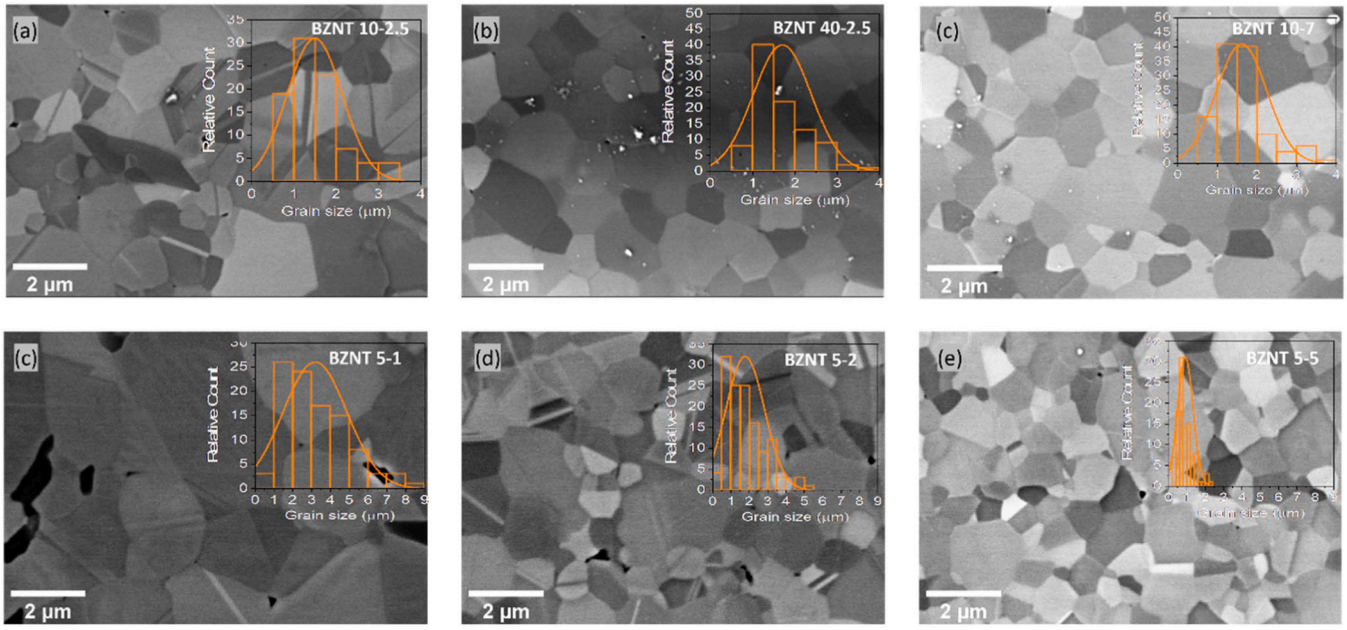

Fig. 2. SEM Images and corresponding grain size distribution of BZNT ceramics: (a) x = 10 % and y = 2.5 %; (b) x = 40 % and y = 2.5 %; (c) x = 10 %, and y = 7 %; (d) x = 5 % and y = 1 %; (e) x = 5 % and y = 2 %; (f) x = 5 % and y = 5 %.

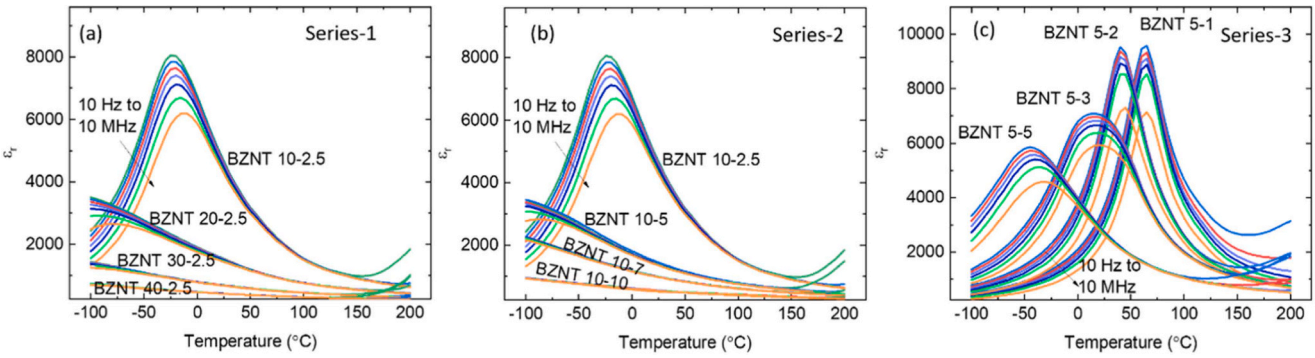

Fig. 3. (a-c) Temperature-dependent relative permittivity at different frequencies of BZNT samples for Series-1, Series-2, and Series-3, respectively.

ceramics exhibited no frequency dependence in the ε_m peak, indicative of the absence of relaxor behavior, whereas the broad appearance of the ε_m peak is compatible with a DPT behavior [12]. The ε_m peaks of BZNT 5–1 and BZNT 5–2 were observed at 60 °C and 30 °C, respectively. With a further increase in Nb from 3 % to 5 %, the ε_m peak shifted below RT and displayed frequency-dispersion characteristics, confirming the presence of relaxor behavior.

To elucidate the transition from conventional FE to relaxors in Series-3 samples, the diffusivity of dielectric properties was explored, as depicted in Fig. 4a-d. In general, according to the Curie-Weiss law, conventional FE adhere to $T_C < T$, while relaxor behavior deviates from this ideal [28]. For a deeper understanding of this phenomenon, the reciprocal of the dielectric constant ($1/\varepsilon_r$) as a function of temperature at 10 kHz was examined for Series-3 ceramics. The Burns temperature (T_B, the temperature at which polar regions on a nanometer scale, characterized by randomly distributed directions of dipole moments, begin to emerge as the sample cools down [29]), was found to gradually increase from 85 °C to 105 °C with increasing Nb substitution in Series-3, expect for the BZNT 5–5 ceramic. For temperatures higher than T_B, the reciprocal permittivity follows the Curie-Weiss law with a linear dependency, which is best described as a paraelectric state of the material [30].

To delve further into the diffuseness of the phase transition within Series-3, a modified Curie-Weiss law was employed to estimate the degree of diffuseness, as follows:

$$\frac{1}{\varepsilon} - \frac{1}{\varepsilon_m} = \frac{(T - T_m)^\gamma}{C_2}$$

Here, ε_m, C_2, and γ represent the maximum dielectric permittivity, the Curie constant, and the degree of diffuseness, respectively. For the evaluation of γ values, we analyzed the plot of $\ln(1/\varepsilon - 1/\varepsilon_m)$ versus $\ln(T - T_m)$ shown in the insets of Fig. 4a-d. The γ values were determined from the slope of the best-fit lines and amounted to 1.57, 1.68, 1.92, and 1.81 for BZNT 5–1, BZNT 5–2, BZNT 5–3, and BZNT 5–5, respectively. It becomes evident that the γ value increases with increased Nb substitution concentration. In accordance with this model, a γ value close to '1' signifies a normal FE material, while '2' aligns with the ideal relaxor [30,31]. As such, the BZNT 5–3 and BZNT 5–5 samples exhibit larger γ values compared to BZNT 5–1 and BZNT 5–2, consistent with an enhanced relaxor behavior. In Fig. 3c, the γ value does not consistently increase with increased Nb substitution concentration, as evidenced by the lower γ value for BZNT 5–5 compared to BZNT 5–3. The complex behavior observed in BZNT 5–3, due to its broader ε_m peak and the mixture of two FE crystal symmetries, may account for its higher γ value. This suggests that factors other than just Nb concentration, such as the nature of the polymorphic phases present, play a significant role in

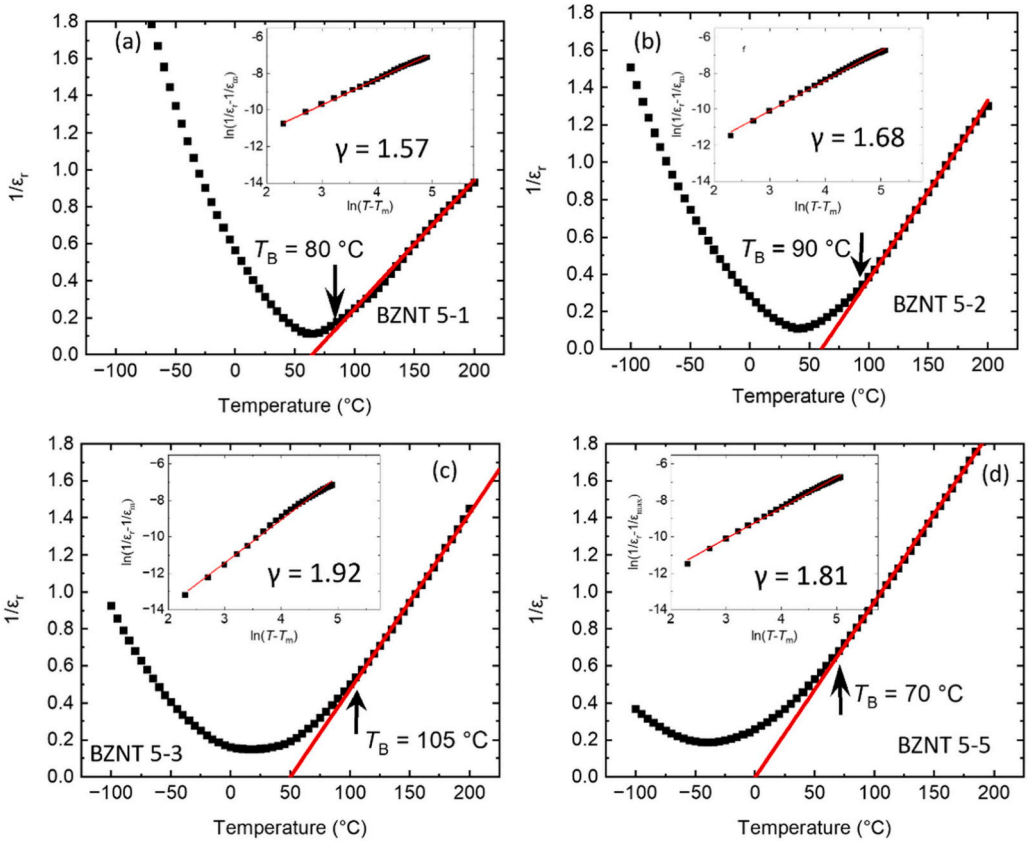

Fig. 4. (a-d) Curie-Weiss plot with marked Burns temperature (T_B) with corresponding inset figures representing the plots of $\ln(1/\varepsilon - 1/\varepsilon_m)$ versus $\ln(T - T_m)$ at 1 kHz for BZNT 5–1, BZNT 5–2, BZNT 5–3 and BZNT 5–5 samples, respectively.

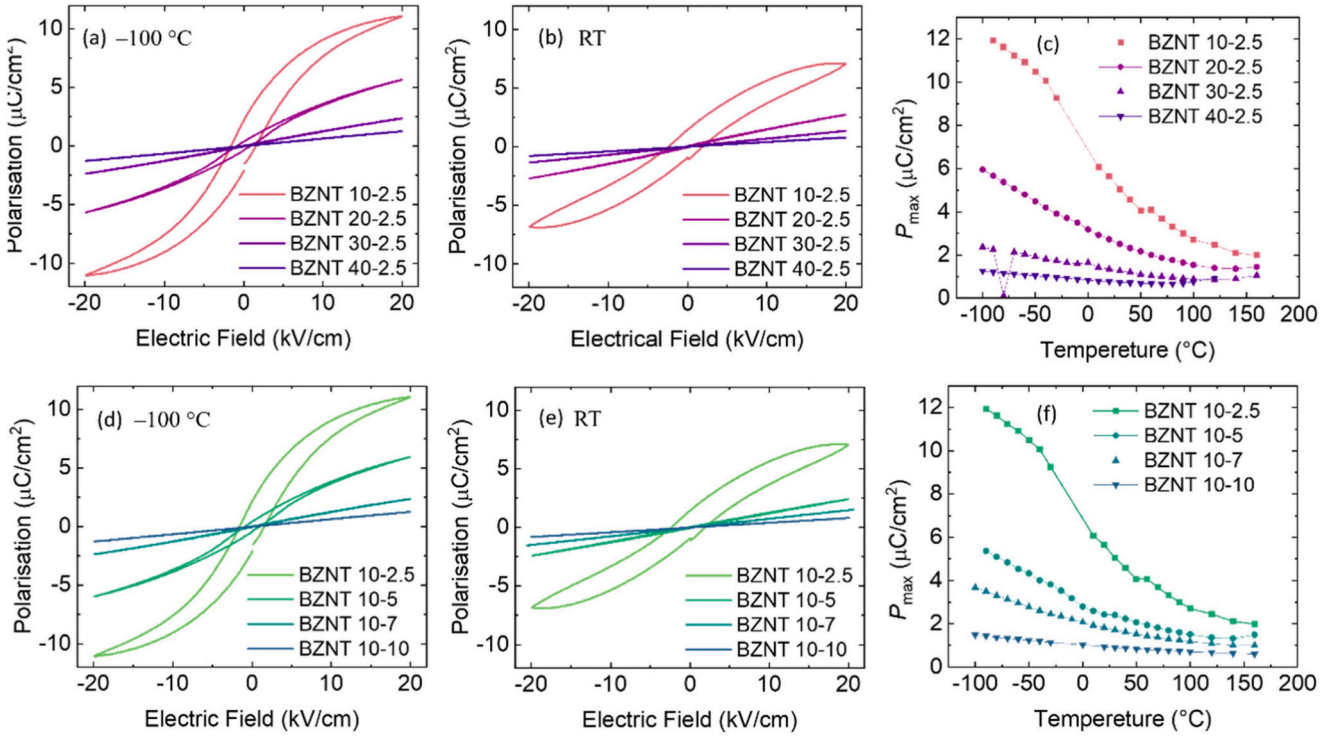

Fig. 5. Polarization-Electric field (P-E) loops of Series-1 samples measured at (a) −100 °C and (b) RT. (c) Temperature-dependent maximum polarization (P_{max}) values of Series-1 samples. P-E loops of Series-2 samples measured at (d) −100 °C and (e) RT. (f) Temperature-dependent P_{max} values of Series-2 samples.

determining the γ value.

To further investigate the electrical characteristics, temperature-dependent *P-E* hysteresis loops were measured for the ceramic samples in Series-1 and Series-2 at a frequency of 10 Hz, as presented in Fig. 5. Notably, the initial ceramic samples of both series, represented by BZNT 10–2.5, displayed rather slim hysteresis loops without a well-saturated polarization at both –100 °C and RT, as depicted in Fig. 5a-b, respectively. This characteristic slim hysteresis behavior aligns with the typical attributes of a relaxor FE, consistent with our frequency-dependent ε_r(T) measurements. The temperature-dependent maximum polarization (P_{max}) for Series-1 is illustrated in Fig. 5c. As anticipated, the P_{max} values exhibited a trend corresponding to the ε_r measurements in Fig. 3a. With an increase in Zr substitution from 10 % to 40 % in Series-1, the P_{max} value dramatically decreased from 5.6 μC/cm^2 to 1.1 μC/cm^2 at RT, indicative of an increase in disorder within the samples, leading to fewer polarizable regions. In fact, the samples with the highest substituent content (BZNT 30–2.5 and BZNT 40–2.5) displayed paraelectric behavior at RT, consistent with the XRD analysis. The temperature-dependent P_{max} values of Series-2 closely mirrored the behavior observed in Series-1. With an increase in Nb substitution from 2.5 % to 10, the P_{max} values diminished from 5.6 μC/cm^2 to 1.0 μC/cm^2 at RT. The remnant polarization (P_r) profiles as functions of temperature for Series-1 and Series-2 are illustrated in Figure S3 of the SI. In the case of BZNT 10–2.5 ceramic, a slight increase in P_r was observed with decreasing temperature, suggesting the presence of a short-range FE ordering at low temperatures. However, as Zr substitution exceeded 10 % in Series-1, P_r decreased from ~1.0 μC/cm^2 to ~0.1 μC/cm^2 at RT and exhibited minimal temperature dependence. A similar trend was observed in Series-2 samples, where P_r decreased from ~1.0 μC/cm^2 to ~0.1 μC/cm^2 at RT with Nb content exceeding 2.5 %, showing little temperature dependency. These findings emphasize that Series-1 and 2 ceramics, excluding BZNT 10–2.5, possess highly disordered structures, resulting in local pseudocubic phase and corresponding paraelectric behavior even at low temperatures (–100 °C).

Within Series-3, the temperature-dependent *P-E* loops of BZNT 5–1 and BZNT 5–2 exhibited saturation polarization with reasonable coercive fields (E_c,) and P_r values at –100 °C, indicative of typical FE behavior, as depicted in Fig. 6a-b. However, increasing Nb substitution from 3 % to 5 %, the *P-E* loops displayed very slim hysteresis with very small P_r and E_c values at RT, signaling the presence of relaxor behavior. These observations align seamlessly with the frequency dispersion in the ε_m peak of BZNT 5–3 and BZNT 5–5 induced by relaxor behavior, as illustrated in Fig. 3c. The increase in Nb substitution from 1 % to 5 % within Series-3 led to a gradual reduction in P_{max} values, diminishing from 12.5 μC/cm^2 to 3.0 μC/cm^2 at RT, providing clear evidence of an increasing disorder within the samples. Furthermore, as the Nb substitution increased, P_r gradually decreased from 3.0 μC/cm^2 to 0.15 μC/cm^2, as illustrated in Figure S3c of the SI. Interestingly, all samples in Series-3, excluding the sample with the highest Nb content (BZNT 5–5), exhibited temperature dependency of P_r, indicating the presence of a local FE crystal symmetry, consistent with XRD analysis. Considering the frequency-dependence of ε_r measurements and the shape of *P-E* loops, it becomes evident that the BZNT ceramic sample featuring 5 % Zr and 3 % Nb displays relaxor behavior at RT. This observation underscores the effectiveness of employing a combination of homovalent and heterovalent substituents, even in relatively small concentration levels, in inducing relaxor behavior.

Fig. 6d and e present the bipolar *S-E* hysteresis loops for Series-3 ceramic samples, taken at –100 °C and RT, respectively, while subjected to an electric field of up to 20 kV/cm. These results illustrate the profound impact of the minor Nb substitution on the electromechanical response. Remarkably, at –100 °C, the bipolar *S–E* curves for BZNT 5–1, BZNT 5–2, and BZNT 5–3 ceramics exhibited a butterfly-like shape with negative strain, as depicted in Fig. 6d. This behavior is characteristic of domain switching in a FE. However, at RT, as seen in Fig. 6e, Series-3 samples displayed slim strain loops without any negative strain, indicative of field-induced strain in an initially non-polar ceramic [4]. The large-signal d_{33}* values, calculated from the strain as a function of temperature, are presented in Fig. 6f. These d_{33}* values exhibited a broad peak-like behavior as a function of temperature, mirroring the

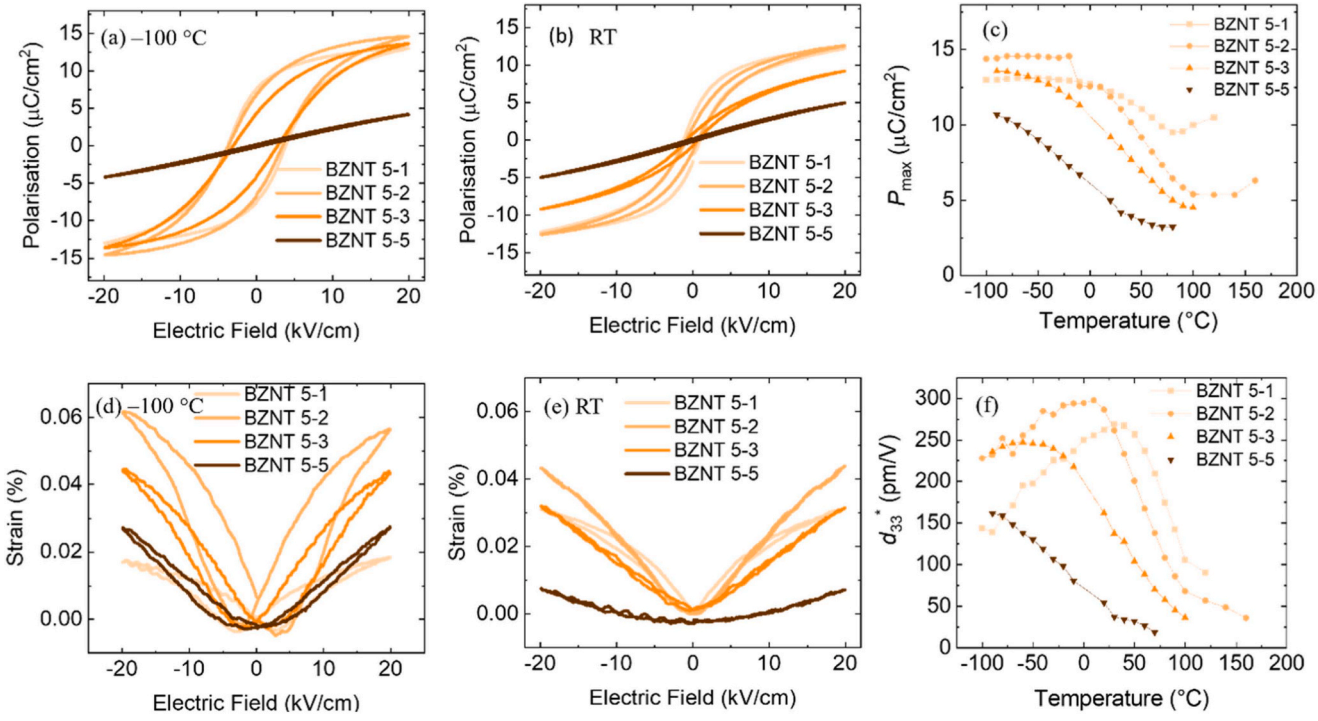

Fig. 6. Polarization-electric field (P-E) loops of Series-3 samples measured at (a) –100 °C and (b) RT. (c) Temperature-dependent maximum polarization (P_{max}) values of Series-1 samples. (d) Electric-field induced strain at (d) –100 °C and (e) RT. (f) Temperature-dependent Large-signal piezoelectric coefficient (d_{33}*) of Series-3 samples.

trends observed in the ε_r measurements presented in Fig. 3c. It is evident that the maximum d_{33}* peak shifted to lower temperatures with increasing Nb substitution in ceramic samples, consistent with the behavior observed in T_m from Fig. 3c. Notably, the BZNT 5–2 sample displayed a maximum d_{33}* value of approximately ~300 pm/V at RT and exhibited substantial d_{33}* values (~250 pm/V) across a broad temperature range (–50 °C to 30 °C). This phenomenon could be attributed to the presence of polymorphic phases in BZNT 5–2, characterized by a narrow temperature range and the associated proximity to FE-relaxor crossover [4,32], a characteristic also supported by the XRD analysis.

Raman spectroscopy stands as an invaluable technique for probing the influence of chemical substitution on the local structure, a factor that can ultimately impact the observed temperature-dependent dielectric response. In Fig. 7, we present the Raman spectra of all series, recorded at RT, with selected Raman modes (from 1 to 6) highlighted as they pertain to lattice disorder in the BZNT ceramics. Within the Raman spectra of Series-1 and 2, as indicated in Fig. 7a and b, no long-range correlation of Ti^{4+} displacements was observed. Typically, in Raman spectroscopy, the presence of long-range correlation of Ti^{4+} displacements would manifest itself as a sharp peak at 311 cm^{-1} (mode 1) and a dip at 180 cm^{-1} (mode 2) [17,20]. The absence of these modes is indicative of the absence of long-range FE polar order in the system [22,33]. Notably, mode 5 (at ~750 cm^{-1}) is associated with ionic radii mismatches attributed to B-site substituents [17]. As the concentration of Zr^{4+} substitution increases in Series-1 ceramics, the intensity of mode 5 also increases and approaches the height of mode 4, signifying random replacement of Ti^{4+} with Zr^{4+} in the BT system (cf. Fig. 7a). Note that mode 4 adheres to first-order Raman scattering rules and is classified as a symmetric octahedral breathing mode in BT ceramics [34]. For Series-2 Raman spectra in Fig. 7b, mode 6 is linked to a localized BO_6 oxygen breathing vibration in the vicinity of Ti vacancies and is thus associated with the presence of V''''_{Ti}-4 Nb^{5+} defect complexes, which emerge as a charge compensation mechanism in BZNT ceramics [7,20]. With an increase in Nb^{5+} substitution concentration, the intensity of mode 6 gradually rises, indicating an increase in V''''_{Ti} concentration within the sublattice. Raman spectra in Fig. 7a and b clearly reveal a high degree of disorder in the Series-1 and 2 ceramics, even in the case of the lowest-substituted sample, namely BZNT 10–2.5. This observation is in accord with dielectric measurements and XRD analyses.

On the other hand, the Raman spectra of Series-3 samples (presented in Fig. 7c), specifically BZNT 5–1 and BZNT 5–2 ceramics, exhibit a distinct rather sharp peak at ~311 cm^{-1} (mode 1) and a small dip at ~180 cm^{-1} (mode 2). As mentioned, these characteristics signify the presence of long-range correlation of Ti^{4+} displacements, reminiscent of the typical FE behavior observed in BT ceramics [22]. With an increase in Nb^{5+} substitution beyond 3 %, mode 6 peak becomes evident as well as the absence of modes 1 and 2, indicating the presence of V''''_{Ti} within the sublattice. This observation aligns seamlessly with the frequency dispersion behavior illustrated in Fig. 3c, where samples with more than 3 % of Nb^{5+} displayed relaxor behavior with short-range polar ordering. Temperature-dependent Raman measurements were conducted for BZNT 5–1, BZNT 5–2, and BZNT 10–2.5, as depicted in Figure S4 of the SI. The BZNT 5–1 and BZNT 5–2 ceramics exhibit FE Raman modes (sharp peak at ~311 cm^{-1} and a small dip at ~180 cm^{-1}) until 100 °C for 1 % Nb and 60°C for 2 % Nb. This indicates the presence of FE-paraelectric phase transition in BZNT 5–1 and BZNT 5–2 samples at 100 °C and 60°C, respectively, as illustrated in Figure S4a and b in the SI, and is in accord with the dielectric measurements in Fig. 3c, which show the permittivity peak below those temperatures. In contrast, the BZNT 10–2.5 ceramic shows no indications of phase transitions, and typical FE features (modes 1 and 2) are absent at all temperatures, suggesting a persistent disruption of long-range FE order and high disorder in the ceramic, which is shown in Figure S4c of SI.

We have summarized the ε_r, P_{max}, and d_{33}* values for all our samples within the compositional range of $BaTiO_3$–$BaZrO_3$–$BaNbO_3$, as illustrated in Fig. 8 with color-coded data markers superimposed on the ternary phase diagram. Note that $BaNbO_3$ is a fictitious compound, and its use in the ternary diagram is just for the sake of consistency in naming. The accompanying bar next to the phase diagram correlates the color of the data marker with the magnitude of (a) ε_r, (b) P_{max}, and (c) d_{33}* at RT. The highest ε_r is observed in the region with 20 % Zr and 0 % Nb, attributed to the proximity of the temperature (T_m) at which the ε_r (7500) maximum occurs to RT, typically forming either a tetragonal phase or a coexistence of tetragonal and orthorhombic phases [7]. Another region of the diagram with high permittivity, however, is in correspondence of the compositions with 5 % Zr and up to 2 % Nb, which are associated also with superior piezoelectric properties. Notably, the BT ceramic with 5 % Zr and 2 % Nb (BZNT 5–2) exhibits the highest P_{max} (11.87 μC/cm^2) and d_{33}* (287 pm/V) properties. Furthermore, it is evident that a slight increase in Nb content beyond 2 % along the 5 % Zr line in the ternary diagram results in a decrease in ε_r, P_{max}, and d_{33}* values. This underscores that even a relatively small concentration of Nb can induce significant changes in piezoelectric and dielectric properties. Along the 5 % Zr line in the ternary diagram, a gradual increase in Nb up to 2 % leads to a broadening of the transition T_C or T_m range, resulting in a DPT and corresponding composition-induced FE-relaxor crossover behavior at RT, which might be responsible for the highest P_{max} value in BZNT 5–2 ceramic solid solution. Furthermore, the XRD and Raman analyses of BZNT 5–2 sample indicate the existence of long-range FE phase transitions and nanoscale structural heterogeneity. These distinctive features in BZNT 5–2 may contribute to additional energy contributions, including electrostatic and elastic energies associated with the presence of heterogeneous interfaces within the ceramic bulk [4,35]. These energies may contribute to further flattening the energy landscape, in addition to the long-range FE phase transitions, thereby potentially accounting for the exceptional piezoelectric properties observed in the BZNT 5–2 sample.

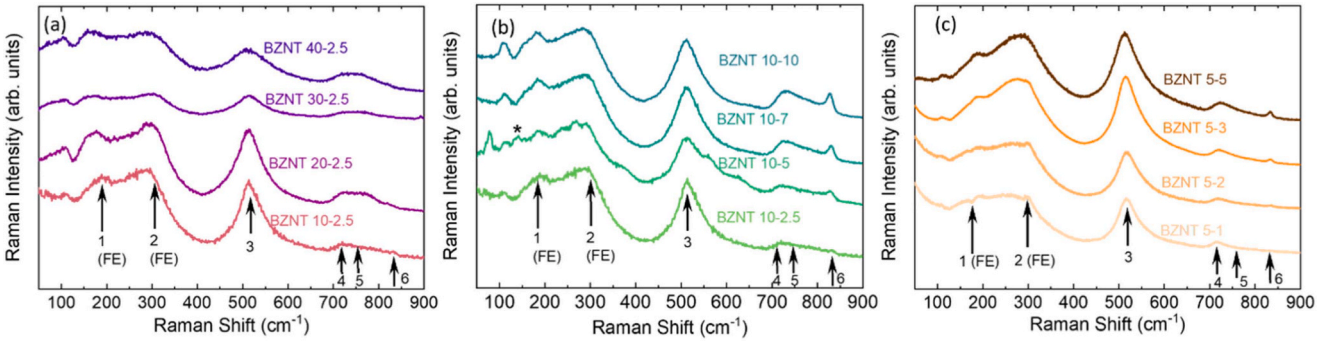

Fig. 7. Room temperature Raman spectra of (a) Series-1, (b) Series-2, and (c) Series-3 of BZNT samples. The peak marked with an asterisk for the BZNT 10–5 composition denotes the secondary phase.

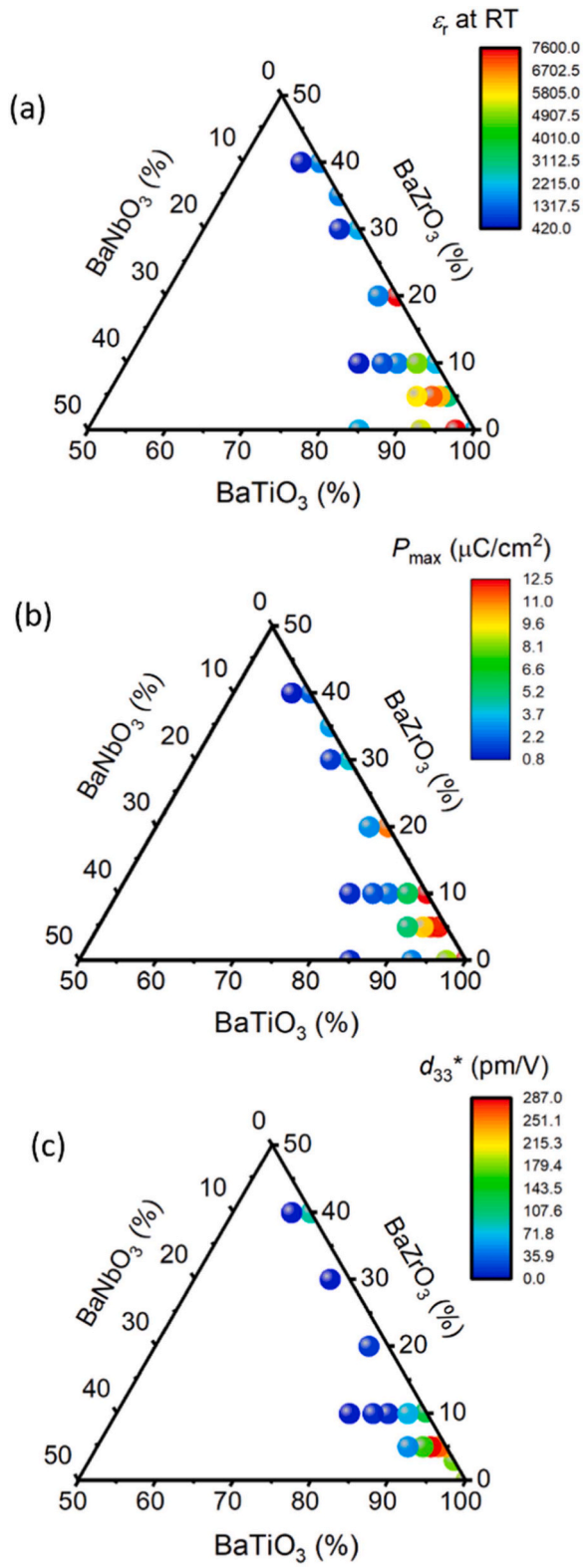

Fig. 8. The triangle ternary diagram of $BaTiO_3$–$BaNbO_3$– $BaZrO_3$ shows (a) Ɛr, (b) P_{max}, (c) d_{33}* at RT.

This phenomenon may contribute to the observed highest d_{33}* values in these samples and will be subject of dedicated investigations in the future. Furthermore, a small increase in Nb substitution from 2 % to 3 % along the 5 % Zr line can lead to fully relaxor behavior in BZNT 5–3 ceramic with relatively the highest ε_r (6929) and P_{max} (9.92 μC/cm^2) compared to single-substituted relaxors with minimal substitution concentration (i.e., BZrT 35 and BNbT 7).

The effectiveness of simultaneous Zr/Nb substitution in BT ceramic is evident in the above ternary diagram. This can be comprehended through the different mechanisms at play in the local disorder and polar ordering of those ceramics, which is schematically shown in Fig. 9a-c. In homovalent (BZrT) ceramics, Zr substitution introduces non-polar strain-based RF regions (depicted in yellow shadings in Fig. 9a), which have a weak and highly localized effect around the Zr atoms. Consequently, a large amount of Zr substitution is required to induce relaxor behavior. This extensive Zr substitution in BT ceramic fosters a fragmented short-range polar state below T_B without complex defects in the lattice (see Fig. 9a, bottom panels). The greater chemical stability of Zr ions reduces electron jumps between Ti^{4+} and Ti^{3+}, resulting in limited dielectric losses in the BZrT ceramics [36,37]. This is exemplified in BZrT 20 ceramic, where the maximum ε_r value at RT was observed in the ternary diagram in Fig. 7a. On the other hand, heterovalent BNbT ceramics contain V'''_{Ti} −4 Nb^{5+} defects, promoting the formation of robust polar RF regions (depicted in red shadings in Fig. 9b). These regions interact with external electric fields on a larger length scale in the lattice, making them more effective in disrupting Ti-O long-range correlation even with a small amount of Nb% substitution content, as experimentally demonstrated in our previous studies [7,20]. In contrast to BZrT, Nb substitution in BT ceramic promotes a highly disordered FE state with nanoscopic polar regions below T_B as well as complex defects in the lattice (see Fig. 9b, bottom panels), giving rise to high dielectric losses [7,38].

In the context of double substituted BZNT ceramics (refer to Fig. 9c), a carefully chosen 5 % Zr content promotes non-polar regions with weak strain-based RFs (yellow shadings), while Nb content generates robust polar RFs (red shadings) that interact with external electric fields on a larger length scale, influencing the long-range spatial correlation of Ti-cation displacements. Consequently, these non-polar regions resulting from Zr substitution can minimize the dielectric losses by shielding charged defects. Moreover, the relatively low levels of Zr and Nb content in mixed BZNT contribute to a reduction in the lattice defect complex, fostering relaxor behavior with a broad and high permittivity response resulting from multiple (Zr- and Nb-based) relaxation processes. This phenomenon is clearly manifested in BZNT 5–3 ceramic, where relaxor behavior is observed with a relatively large ε_r and slim *P-E* loops, exhibiting the highest P_{max} value compared to single-substituted BZrT 35 and BNbT 7 relaxors with minimal substitution concentration [7]. This observation underscores the efficacy of employing a combination of homovalent (Zr) and heterovalent (Nb) substitutions to induce relaxor behavior in lead-free BT ceramics, achieving high permittivity and a substantial P_{max} value, which is essential for attaining attractive dielectric properties, such as – for instance – for energy storage applications. Furthermore, this combination of substituents (remarkably for Nb contents below 3 %, for which FE phase is present) appears to promote high piezoelectric properties that are stable over a large temperature interval (–50 °C to 30 °C), which makes these materials attractive for underwater applications or in-body applications, especially considering the biocompatibility of BT-based compositions.

4. Conclusion

In summary, this comprehensive investigation into simultaneous homovalent (Zr) and heterovalent (Nb) substitution in lead-free BT perovskite ceramics has yielded valuable insights into their structural, microstructural, and electrical characteristics. XRD analysis indicated the formation of a single-phase perovskite solid solution, revealing an increase in lattice parameters with increasing Zr or Nb content across all ceramic series. Series-3 samples displayed a mixture of perovskite phases with different crystal symmetries, as unveiled by XRD refinement. The temperature-dependent ε_m behavior in Series-1 and 2 ceramics

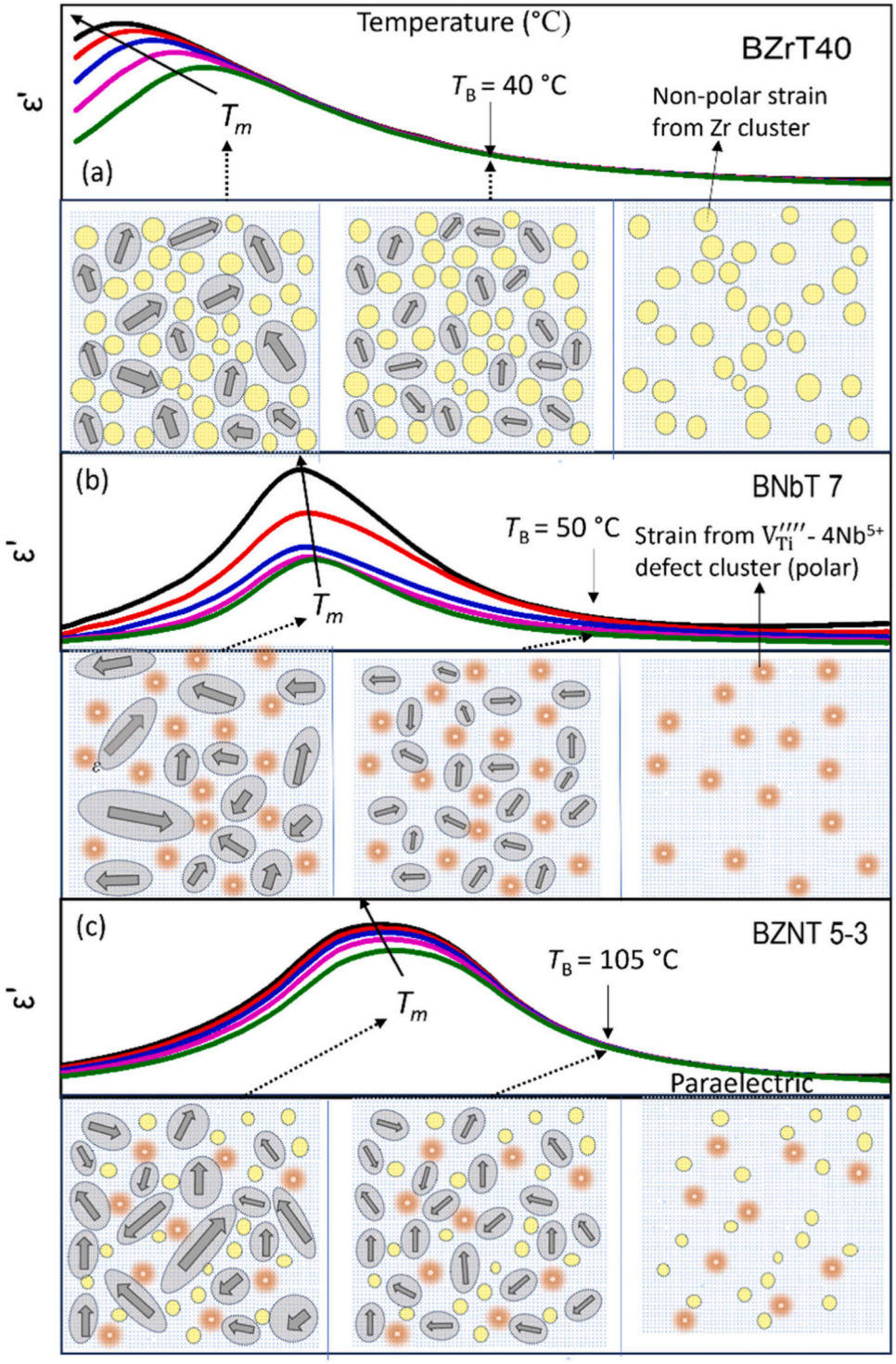

Fig. 9. Proposed temperature-dependent evolution of local disorder and polar ordering in (a) BZrT 40, (b) BNbT 7, and (c) BZNT 5–3 relaxors.

showed frequency dispersion mostly below RT, with the ε_m peak shifting to lower temperatures as Zr or Nb content increased. Remarkably, in Series-3, specifically in BZNT samples with a constant 5 % Zr and increasing Nb from 1 % to 2 %, the ε_m peak extended at and above RT with DPT and no relaxor behavior. The BZNT 5–3 ceramic exhibited relaxor behavior at relatively low concentrations (5 % Zr and 3 % Nb), corroborated by frequency-dependent ε_r measurements and modified Curie-Weiss law analyses. Furthermore, this relaxor composition exhibited higher permittivity and maximum polarization than single-substituted BZrT 35 or BNbT 7 relaxors, which makes it very interesting for dielectric applications. Notably, BT ceramics with 5 % Zr and 2 % Nb substitution displayed substantial d_{33}* values (~250 pm/V) observed across a broad temperature range (–50°C to 30°C). This enhancement is likely due to the presence of polymorphic phases in BZNT 5–2, characterized by a narrow temperature range and proximity to the FE-relaxor crossover. This unique characteristic makes the BZNT 5–2 composition particularly promising for piezoelectric applications. The proposed schematic representation of non-polar and polar lattice structures induced by Zr and Nb substituents, respectively, emphasizes the effectiveness of simultaneous Zr/Nb substitution in disrupting long-

range FE behavior and attaining interesting properties. This investigation underscores the responsiveness of piezoelectric and dielectric properties to minute concentrations of Nb/Zr within the ternary phase diagram, paving the way for the customized tailoring of properties in lead-free BT ceramics for specific applications.

Author contribution

Conceptualization and planning of the work was carried out by M.D. with the support of V. R. N.; C.M. and V.R.N prepared the samples with the support of K.R. XRD and dielectric permittivity measurements were performed by K.R.; Temperature-dependent Raman measurements were performed by J.G., V.R.N. and M.D.; Temperature-dependent polarization and strain loops measured by V.R.N. with the support of A.F.; The manuscript was written by V.R.N. and revised by M.D., A.F. and K.R.

CRediT authorship contribution statement

Venkata Raveendra Nallagatla: Writing – original draft, Methodology, Data curation, Conceptualization. **Christian Maier:** Methodology. **Jürgen Glettler:** Methodology. **Antonio Feteira:** Writing – review & editing. **Klaus Reichmann:** Writing – review & editing, Methodology. **Marco Deluca:** Writing – review & editing, Supervision, Funding acquisition, Conceptualization.

Declaration of Competing Interest

The authors declare that they have no known competing financial interests or personal relationships that could have appeared to influence the work reported in this paper.

Acknowledgments

This project has received funding from the Austrian Science Fund (FWF): Project I4581-N. M.D. acknowledges also support from the European Research Council (ERC) under the European Union's Horizon 2020 research and innovation program (grant agreement No 817190).

Appendix A. Supporting information

Supplementary data associated with this article can be found in the online version at doi:10.1016/j.jeurceramsoc.2024.116689.

References

[1] H.D. Megaw, Crystal structure of barium titanate, Nature 155 (1945) 484–485, https://doi.org/10.1038/155484B0 [9].
[2] K.I. Sakayori, Y. Matsui, H. Abe, E. Nakamura, M. Kenmoku, T. Hara, D. Ishikawa, A. Kokubu, K.I. Hirota, T. Ikeda, Curie temperature of baTiO3, Jpn J. Appl. Phys. 34 (1995) 5443–5445, https://doi.org/10.1143/JJAP.34.5443/XML.
[3] V.V. Lemanov, Barium titanate-based solid solutions, Ferroelectrics 354 (2007) 69–76, https://doi.org/10.1080/00150190701454545.
[4] M. Acosta, N. Novak, V. Rojas, S. Patel, R. Vaish, J. Koruza, G.A. Rossetti, J. Rödel, BaTiO3-based piezoelectrics: fundamentals, current status, and perspectives, Appl. Phys. Rev. 4 (2017) 41305, https://doi.org/10.1063/1.4990046/123894.
[5] V. Veerapandiyan, F. Benes, T. Gindel, M. Deluca, Strategies to improve the energy storage properties of perovskite lead-free relaxor ferroelectrics: a review, 2020, Vol. 13, Page 5742, Materials 13 (2020) 5742, https://doi.org/10.3390/MA13245742.
[6] V. Buscaglia, C.A. Randall, Size and scaling effects in barium titanate. An overview, J. Eur. Ceram. Soc. 40 (2020) 3744–3758, https://doi.org/10.1016/J.JEURCERAMSOC.2020.01.021.
[7] V. Veerapandiyan, M.N. Popov, F. Mayer, J. Spitaler, S. Svirskas, V. Kalendra, J. Lins, G. Canu, M.T. Buscaglia, M. Pasciak, J. Banys, P.B. Groszewicz, V. Buscaglia, J. Hlinka, M. Deluca, V. Veerapandiyan, M.N. Popov, F. Mayer, J. Spitaler, M. Deluca, S. Svirskas, V. Kalendra, J. Banys, J. Lins, P.B. Groszewicz, M. Pasciak, J. Hlinka, Origin of relaxor behavior in barium-titanate-based lead-free perovskites, Adv. Electron Mater. 8 (2022) 2100812, https://doi.org/10.1002/AELM.202100812.
[8] J. Liu, L. Liu, J. Zhang, L. Jin, D. Wang, J. Wei, Z.G. Ye, C.L. Jia, Charge effects in donor-doped perovskite ferroelectrics, J. Am. Ceram. Soc. 103 (2020) 5392–5399, https://doi.org/10.1111/JACE.17270.
[9] R. Farhi, M. El Marssi, A. Simon, J. Ravez, Relaxor-like and spectroscopic properties of niobium modified barium titanate, Eur. Phys. J. B 18 (2000) 605–610, https://doi.org/10.1007/S100510070008/METRICS.
[10] C. Laulhé, F. Hippert, J. Kreisel, A. Pasturel, A. Simon, J.L. Hazemann, R. Bellissent, G.J. Cuello, Random local strain effects in the relaxor ferroelectric BaTi 1-xZrxO3: experimental and theoretical investigation, Phase Transit. 84 (2011) 438–452, https://doi.org/10.1080/01411594.2010.547153.
[11] A. Von Hippel, Ferroelectricity, domain structure, and phase transitions of barium titanate, Rev. Mod. Phys. 22 (1950) 221, https://doi.org/10.1103/revmodphys.22.221.
[12] G. Smolensky, Ferroelectrics with diffuse phase transition, Ferroelectrics 53 (1984) 129–135, https://doi.org/10.1080/00150198408245041.
[13] V.K. Veerapandiyan, M. Deluca, S.T. Misture, W.A. Schulze, S.M. Pilgrim, S. C. Tidrow, Dielectric and structural studies of ferroelectric phase evolution in dipole-pair substituted barium titanate ceramics, J. Am. Ceram. Soc. 103 (2020) 287–296, https://doi.org/10.1111/JACE.16713.
[14] V.V. Shvartsman, D.C. Lupascu, Lead-free relaxor ferroelectrics, J. Am. Ceram. Soc. 95 (2012) 1–26, https://doi.org/10.1111/J.1551-2916.2011.04952.X.
[15] A. Pramanick, S. Nayak, Perspective on emerging views on microscopic origin of relaxor behavior, J. Mater. Res. 36 (2021) 1015–1036, https://doi.org/10.1557/S43578-020-00010-7/METRICS.
[16] A. Anju Balaraman, S. Dutta, Inorganic dielectric materials for energy storage applications: a review, J. Phys. D. Appl. Phys. 55 (2022) 183002, https://doi.org/10.1088/1361-6463/AC46ED.
[17] V. Buscaglia, S. Tripathi, V. Petkov, M. Dapiaggi, M. Deluca, A. Gajović, Y. Ren, Average and local atomic-scale structure in BaZrxTi1-xO 3 (x = 0.10, 0.20, 0.40) ceramics by high-energy x-ray diffraction and Raman spectroscopy, J. Phys. Condens. Matter 26 (2014), https://doi.org/10.1088/0953-8984/26/6/065901.
[18] H.M. Chan, M.R. Harmer, D.M. Smyth, Compensating defects in highly donor-doped BaTiO3, J. Am. Ceram. Soc. 69 (1986) 507–510, https://doi.org/10.1111/J.1151-2916.1986.TB07453.X.
[19] T. Dechakupt, J. Tangsritrakul, P. Ketsuwan, R. Yimnirun, Microstructure and electrical properties of niobium doped barium titanate ceramics, Ferroelectrics 415 (2011) 141–148, https://doi.org/10.1080/00150193.2011.577386.
[20] V.K. Veerapandiyan, S. Khosravi H, G. Canu, A. Feteira, V. Buscaglia, K. Reichmann, M. Deluca, B-site vacancy induced Raman scattering in BaTiO3-based ferroelectric ceramics, J. Eur. Ceram. Soc. 40 (2020) 4684–4688, https://doi.org/10.1016/J.JEURCERAMSOC.2020.05.051.
[21] T. Rojac, D. Damjanovic, Domain walls and defects in ferroelectric materials, Jpn J. Appl. Phys. 56 (2017) 10PA01, https://doi.org/10.7567/JJAP.56.10PA01/XML.
[22] M. Deluca, H. Hu, M.N. Popov, J. Spitaler, T. Dieing, Advantages and developments of Raman spectroscopy for electroceramics, 2023 4:1, Commun. Mater. 4 (2023) 1–15, https://doi.org/10.1038/s43246-023-00400-4.
[23] E. Brzozowski, M.S. Castro, Grain growth control in Nb-doped BaTiO3, J. Mater. Process Technol. 168 (2005) 464–470, https://doi.org/10.1016/J.JMATPROTEC.2005.02.246.
[24] O. Eibl, P. Pongratz, P. Skalicky, H. Schmelz, Formation of (111) Twins in BaTiO3 Ceramics, –C195, J. Am. Ceram. 70 (1987) C195, https://doi.org/10.1111/j.1151-2916.1987.tb05724.x.
[25] B.K. Lee, S.Y. Chung, S.J.L. Kang, Control of {111} twin formation and abnormal grain growth in BaTio3, Met. Mater. Int. 6 (2000) 301–304, https://doi.org/10.1007/BF03028075/METRICS.
[26] B.K. Lee, S.Y. Chung, S.J.L. Kang, Grain boundary faceting and abnormal grain growth in BaTiO3, –1575, Acta Mater. 48 (2000) 1575, https://doi.org/10.1016/s1359-6454(99)00434-6.
[27] E. Brzozowski, M.S. Castro, C.R. Foschini, B. Stojanovic, Secondary phases in Nb-doped BaTiO3 ceramics, Ceram. Int. 28 (2002) 773–777, https://doi.org/10.1016/S0272-8842(02)00042-1.
[28] R.A. Cowley, S.N. Gvasaliya, S.G. Lushnikov, B. Roessli, G.M. Rotaru, Relaxing with relaxors: a review of relaxor ferroelectrics, Adv. Phys. 60 (2011) 229–327, https://doi.org/10.1080/00018732.2011.555385.
[29] A.A. Bokov, Z.G. Ye, Recent progress in relaxor ferroelectrics with perovskite structure, J. Mater. Sci. 41 (2006) 31–52, https://doi.org/10.1007/S10853-005-5915-7/METRICS.
[30] L.E. Cross, Relaxor ferroelectrics: an overview, Ferroelectrics 151 (1994) 305–320, https://doi.org/10.1080/00150199408244755.
[31] D. Viehland, S.J. Jang, L.E. Cross, M. Wuttig, Deviation from Curie-Weiss behavior in relaxor ferroelectrics, Phys. Rev. B 46 (1992) 8003, https://doi.org/10.1103/PhysRevB.46.8003.
[32] A.J. Bell, O. Deubzer, Lead-free piezoelectrics - the environmental and regulatory issues, MRS Bull. 43 (2018) 581–587, https://doi.org/10.1557/MRS.2018.154/METRICS.
[33] M.N. Popov, J. Spitaler, V.K. Veerapandiyan, E. Bousquet, J. Hlinka, M. Deluca, Raman spectra of fine-grained materials from first principles, 2020 6:1, NPJ Comput. Mater. 6 (2020) 1–7, https://doi.org/10.1038/s41524-020-00395-3.
[34] R. Farhi, M. El Marssi, A. Simon, J. Ravez, A Raman and dielectric study of ferroelectric Ba(Ti1-xZrx)O3 ceramics, Eur. Phys. J. B 9 (1999) 599–604, https://doi.org/10.1007/S100510050803/METRICS.
[35] F. Li, S. Zhang, D. Damjanovic, L.-Q. Chen, T.R. Shrout, F. Li, S. Zhang, L.-Q. Chen, T.R. Shrout, S.J. Zhang, D. Damjanovic, Local structural heterogeneity and electromechanical responses of ferroelectrics: learning from relaxor ferroelectrics, Adv. Funct. Mater. 28 (2018) 1801504, https://doi.org/10.1002/ADFM.201801504.
[36] J. Petzelt, V. Bovtun, D. Nuzhnyy, M. Kempa, M. Savinov, M.P. Paściak, S. Kamba, G. Canu, V. Buscaglia, Broadband Dielectric, Terahertz, and Infrared Spectroscopy of BaTiO 3-BaZrO 3 Solid Solution: From Proper Ferroelectric over Diffuse and

Relaxor Ferroelectrics and Dipolar Glass to Normal Dielectric, (2021). https://doi.org/10.1002/pssb.202100259.

[37] M. Reda, S.I. El-Dek, M.M. Arman, Improvement of ferroelectric properties via Zr doping in barium titanate nanoparticles, J. Mater. Sci. Mater. Electron. 33 (2022) 16753–16776, https://doi.org/10.1007/S10854-022-08541-X/TABLES/8.

[38] Y. Jung Kim, J. Won Hyun, H. Soo Kim, J. Ho Lee, M. Young Yun, S.J. Noh, Y. Hyun Ahn, Microstructural Characterization and Dielectric Properties of BaTiO3, 2009.